Check for updates

Zn-Air Batteries

Boric Acid-Assisted Pyrolysis for High-Loading Single-Atom Catalysts to Boost Oxygen Reduction Reaction in Zn-Air Batteries

Chenxi Xu, Jiexing Wu, Liang Chen, Yi Gong, Boyang Mao, Jincan Zhang, Jinhai Deng, Mingxuan Mao, Yan Shi, Zhaohui Hou, Mengxue Cao, Huanxin Li*, Haihui Zhou*, Zhongyuan Huang*, and Yafei Kuang

The emerging of single-atom catalysts (SACs) offers a great opportunity for the development of advanced energy storage and conversion devices due to their excellent activity and durability, but the actual mass production of high-loading SACs is still challenging. Herein, a facile and green boron acid (H₃BO₃)-assisted pyrolysis strategy is put forward to synthesize SACs by only using chitosan, cobalt salt and H₃BO₃ as precursor, and the effect of H₃BO₃ is deeply investigated. The results show that molten boron oxide derived from H₃BO₃ as ideal high-temperature carbonization media and blocking media play important role in the synthesis process. As a result, the acquired Co/N/B tri-doped porous carbon framework (Co-N-B-C) not only presents hierarchical porous structure, large specific surface area and abundant carbon edges but also possesses high-loading single Co atom (4.2 wt.%), thus giving rise to outstanding oxygen catalytic performance. When employed as a catalyst for air cathode in Zn-air batteries, the resultant Co-N-B-C catalyst shows remarkable power density and long-term stability. Clearly, our work gains deep insight into the role of H₃BO₃ and provides a new avenue to synthesis of high-performance SACs.

1. Introduction

To strategically cater for the goals of energy saving and emission reduction, a series of green and sustainable energy storage and conversion devices have been developed. [1,2] Among them, Zn-air batteries (ZABs)

attract worldwide attentions due to their intriguing energy density and high working safety. However, the actual working efficiency of ZABs is always plagued by sluggish oxygen reduction reaction (ORR).^[3,4] As is known to us, noble metal Pt-based catalysts possess outstanding catalytic activity towards ORR, but they suffer from high price and supply uncertainty, which greatly hinder their large-scale commercial application.^[5–7] Therefore, exploring cost-effective ORR catalysts is desperately desired.

Single-atom catalysts (SACs) are widely accepted as potential candidates owing to their maximal utilization of active metal sites. [8,9] Among them, transition metal atoms anchored onto nitrogen-doped carbon materials (M–N–C) are expected to deliver significantly improved intrinsic activity as metal atoms coordinated with N atoms alter the band gap and electronic structure of carbon materials, which is beneficial to reducing the oxygen activation barriers. [10–13]

At present, various approaches have been employed to synthesize M–N–C. From the perspective of practical operability, the wetchemistry route is demonstrated to be more desirable. [14,15] Generally, it involves the steps of dispersing, reducing and anchoring metal precursors. Actually, the synthetic process always confronts with

C. Xu, J. Wu, M. Cao, Prof. H. Li, Prof. H. Zhou, Prof. Z. Huang, Prof. Y. Kuang State Key Laboratory for Chemo/Biosensing and Chemometrics and College of Chemistry and Chemical Engineering, Hunan University, Changsha 410082, China

E-mail: hl583@cam.ac.uk E-mail: haihuizh@hnu.edu.cn E-mail: zhongyhuang@hnu.edu.cn

Dr. L. Chen, Prof. Z. Hou

School of Chemistry and Chemical Engineering, Key Laboratory of Hunan Province for Advanced Carbon-based Functional Materials, Hunan Institute of Science and Technology, Yueyang 414006, China

Y. Gong

Advanced Technology Institute, University of Surrey, Guildford Surrey GU2 7XH, UK

Dr. B. Mao, Dr. J. Zhang, Prof. H. Li

Department of Engineering, University of Cambridge, 9 JJ Thomson Avenue, Cambridge CB3 0FA, UK

Dr. J. Deng, Prof. H. Li

King's College London, London SE1 1UL, UK

Dr. M. Mao

Department of Electrical and Electronic Engineering, Imperial College London, London SW7 2AZ, UK

Dr. Y. Shi

College of Materials and Metallurgy, Guizhou University, Guiyang 550025, China

Prof. H. L

Department of Chemistry, Physical & Theoretical Chemistry Laboratory, University of Oxford, South Parks Road, Oxford OX1 3QZ, UK

The ORCID identification number(s) for the author(s) of this article can be found under https://doi.org/10.1002/eem2.12569.

DOI: 10.1002/eem2.12569

spontaneous aggregation of metal species due to their high surface energy. [16] Therefore, selecting suitable carbon precursors to provide strong interaction between metal precursors and carbon matrix proves much critical.

Biomass, as cheap and abundant carbon resource, is very popular in the field of carbon materials. [17-19] Since the potential heteroatoms (such as N, P, S, etc.) in biomass can coordinate with the metal species, they are always considered as promising carbon precursors for the massive synthesis of M–N–C. [20,21] Although abundant heteroatoms in biomass can absorb and anchor metal ions, the combination force seems not strong enough to achieve atomic dispersion of metal atoms. As a result, parts of metal species will aggregate to form metal particles, which usually leads to low loading (less than 2 wt.%) of isolated single-atom metal sites. [9,22,23] Exploring a feasible way to block the aggregation and thus obtain high-loading M–N–C catalysts still remains a huge challenge. [24–26]

To this end, H₃BO₃-assisted one-step pyrolysis strategy was put forward to synthesize SACs by only employing chitosan, cobalt nitrate and H₃BO₃ as precursor. Herein, the effect of H₃BO₃ was deeply investigated. As is well known, H₃BO₃ will decompose to boron oxide (B₂O₃) through continuous dehydration during constant heating (200-400 °C). While, B₂O₃ with low melting point always presents melting fluidity under conventional carbonization temperature, thus play important role in the synthesis process: 1) High-temperature carbonization media. Biomass precursor of chitosan can be dispersed and carbonized into discontinuous carbon fragments in the molten media. B2O3 media can be removed by simple water rinsing and carbon frameworks with abundant edges and pores can be produced. 2) Blocking media. Molten B2O3 can effectively block Co species from aggregation thus facilitating the formation of single-atom Co sites. As a consequence, the resultant Co/N/B tri-doped porous carbon framework (Co-N-B-C) not only presents hierarchical porous structure, large SSA and abundant exposed edge but also possesses high-loading isolated Co atom (4.2 wt.%). When employed as a catalyst for ORR and air cathode in ZABs, the Co-N-B-C catalyst shows remarkable electrochemical performance. Apart from these, it is highly mentioned that H₃BO₃ can be recycled and reused by recrystallization due to the reaction $(B_2O_3 + H_2O \rightarrow H_3BO_3)$. Undoubtedly, our work provides a green and facile way to fabricate high-performance SACs.

2. Results and Discussion

2.1. Morphology and Structure

The schematic diagram of the preparation of Co–N–B–C is presented in **Figure 1a**. First, appropriate proportion of chitosan, cobalt salt and H_3BO_3 were blended together and then pyrolyzed under high temperature. After the B_2O_3 media was washed away, rich carbon edges and pores can be generated in the resultant Co–N–B–C (see Figure 1b–d). It is worthy to mention that the washed B_2O_3 will be reconverted to H_3BO_3 , and can be reused in the next time, which well follows up the anticipated 3R (reduce, reuse, recycle) principles. [17]

The SEM image of Co–N–B–C in Figure 1b shows fluffy surface and abundant pores. Also, the TEM image in Figure 1c presents that numerous carbon clusters with an average size of several nanometers fold and intertwine with each other. As for the HRTEM image in Figure 1d, it confirms the fact that no metal particles exist in the amorphous carbon derived from chitosan, which may be ascribed to the

blocking effect of H₃BO₃ that it blocks Co species from agglomeration during pyrolysis process. In addition to this, a large number of carbon edges and nanopores marked with red arrows can be discerned from the TEM image. The AC-HAADF-STEM image in Figure 1e displays lots of bright dots in carbon matrix, indicating the uniform distribution of single Co atom. The content of Co determined by inductively coupled plasma mass spectrometry (ICP-MS) is 4.2 wt.%. The EDS elemental mapping images in Figure 1f show that N, B and Co elements are simultaneously doped into carbon matrix, implying successful synthesis of Co-N-B-C. Quite differently, the SEM image of boron-free Co@Co-N-C in Figure S1, Supporting Information delivers relatively compact carbon block without rich pores. Therefore, it is reasonable to deduce that introduced H₃BO₃ makes contribution to the production of abundant edge and pores in carbon matrix. Furthermore, in contrast to the state of Co species in Co-N-B-C, large metal particles can be evidenced in Co@Co-N-C, again verifying the blocking effect of H_3BO_3 .

XRD and Raman techniques were employed to further detect the microstructure of Co-N-B-C and Co@Co-N-C. As shown in the XRD patterns of Figure 2a, Co-N-B-C only shows two typical peaks at $\sim 26^{\circ}$ and ~43°, corresponding to the (002) and (101) crystal faces of carbon. Meanwhile, neither metal Co nor Co-based compound can be witnessed in the XRD pattern of Co-N-B-C, which corresponds to the analysis of TEM image. By contrast, Co@Co-N-C displays obvious metal Co peaks (PDF#15-0806) in the XRD pattern. And it is found that the (002) carbon peak for Co-N-B-C moves to a more negative position than that for Co@Co-N-C, revealing increased interplanar distance caused by the abundant edge upon the carbon surface. [13] The Raman spectra in Figure 2b manifest that the I_D/I_G value for Co–N–B–C (0.87) proves much higher than that for Co@Co-N-C (0.79), indicating higher defect degree. The higher defect degree in Co-N-B-C is closely related to the existence of rich carbon edges and successful B doping.[21,27]

The N₂ adsorption-desorption isothermal curves were conducted to analyze the SSA and pore structure. As depicted in Figure 2c, the SSA of Co–N–B–C (1056.6 $\rm m^2~g^{-1}$) proves much larger than that of Co@Co–N–C (344.8 $\rm m^2~g^{-1}$). The significantly increased SSA can be attributable to fact that the molten B_2O_3 lead to discontinuous carbon fragments, and numerous pores are generated after B2O3 crystal is washed away, which is consistent with previous literature. [28] Obviously, large SSA for Co-N-B-C not only benefits the uniform distribution of Co atoms but also facilitates the exposure of catalytic sites.^[29] As reflected from the pore size distribution curves in Figure 2d, typical mesoporous peak at ~4 nm appears. The mesopores may originate from the decomposition of organic functional groups in chitosan during pyrolysis process. It is demonstrated that rich mesopores offer sufficient channels for electrolyte infiltration and ions transport. [26] Apart from this, it is found that the microporous peak at <2 nm emerges in the curve of Co-N-B-C, implying the existence of abundant micropores, which might be ascribed to B2O3 media enfold and intrude the voids of carbon fragments. Apparently, these abundant micropores in Co-N-B-C is in favor of hosting sufficient catalytic sites towards ORR.^[30,31] Undoubtedly, the micro/meso hierarchical porous structure endows Co-N-B-C with many intriguing features, including large SSA, easy accessibility to electrolyte, fast ions transport, exposure of catalytic sites and so forth.

X-ray photoelectron spectroscopy (XPS) was carried out to explore the chemical composition and element binding state. The XPS survey spectrum of Co–N–B–C in Figure S2, Supporting Information

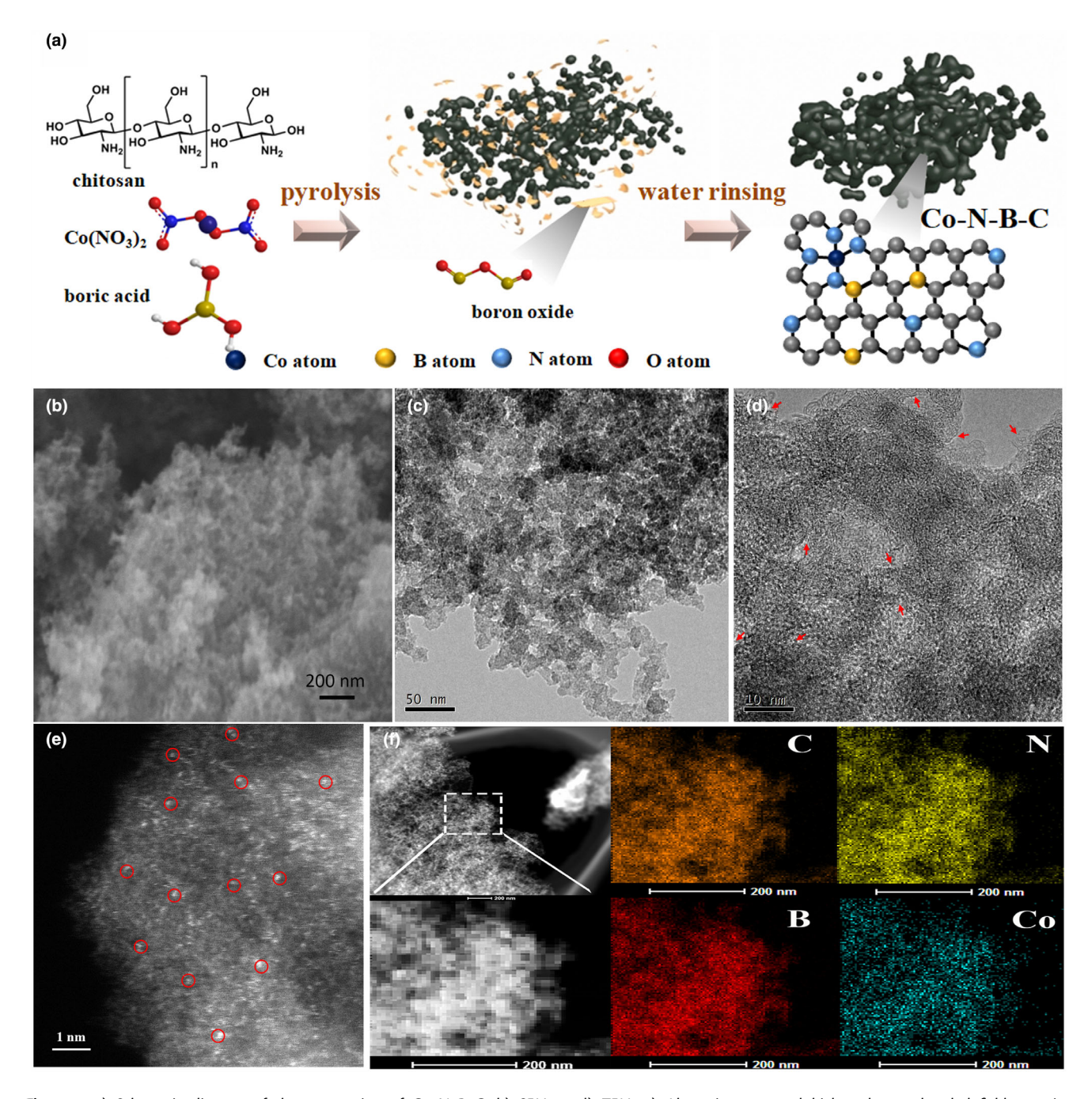


Figure 1. a) Schematic diagram of the preparation of Co–N–B–C. b) SEM, c, d) TEM, e) Aberration-corrected high-angle annular dark-field scanning transmission electron microscopy (AC-HAADF-STEM) image and f) EDS element mappings of Co–N–B–C.

demonstrates the existence of C, N, O, B and Co, indicating Co, N and B tri-doping. As for the electron-accepting B atom, it itself acts as active sites affinitive to oxygen, which makes it easy to detach oxygen. Additionally, its electrophilic nature suffices to alter the surrounding electron structure, thus optimizing the bind energy of other active sites. [32,33] The high-resolution C 1s spectra in Figure 2e can be deconvolved into three well-defined peaks, corresponding to C-sp², C-sp³ and C-O/C=O respectively. Clearly, the proportion of C-sp²/C-sp³ for Co@Co-N-C was calculated to be 4.04, while this value decreases to 2.37 for Co-N-B-C, suggesting more serious damage of sp² graphitic structure in

Co–N–B–C. $^{[27,34]}$ As depicted in the high-resolution N 1 s spectra (Figure S3, Supporting Information), three typical peaks at 398.2 eV, 400.1 eV and 401.6 eV can be assigned to pyridinic-N, pyrrolic-N and graphitic-N, $^{[20,35,36]}$ while the other peak at around 399.2 eV corresponds to the Co–N_x sites. $^{[16]}$ This result can be substantiated by the appearance of Co–N bond (~781.6 eV) in the high-resolution Co 2p spectra (Figure 2f), suggesting that Co species in Co–N–B–C prefers to establish active Co–N_x sites rather than metal Co bulk. $^{[37-39]}$

The chemical state and local structure of Co atom in Co–N–B–C is further explored by X-ray absorption fine structure (XAFS)

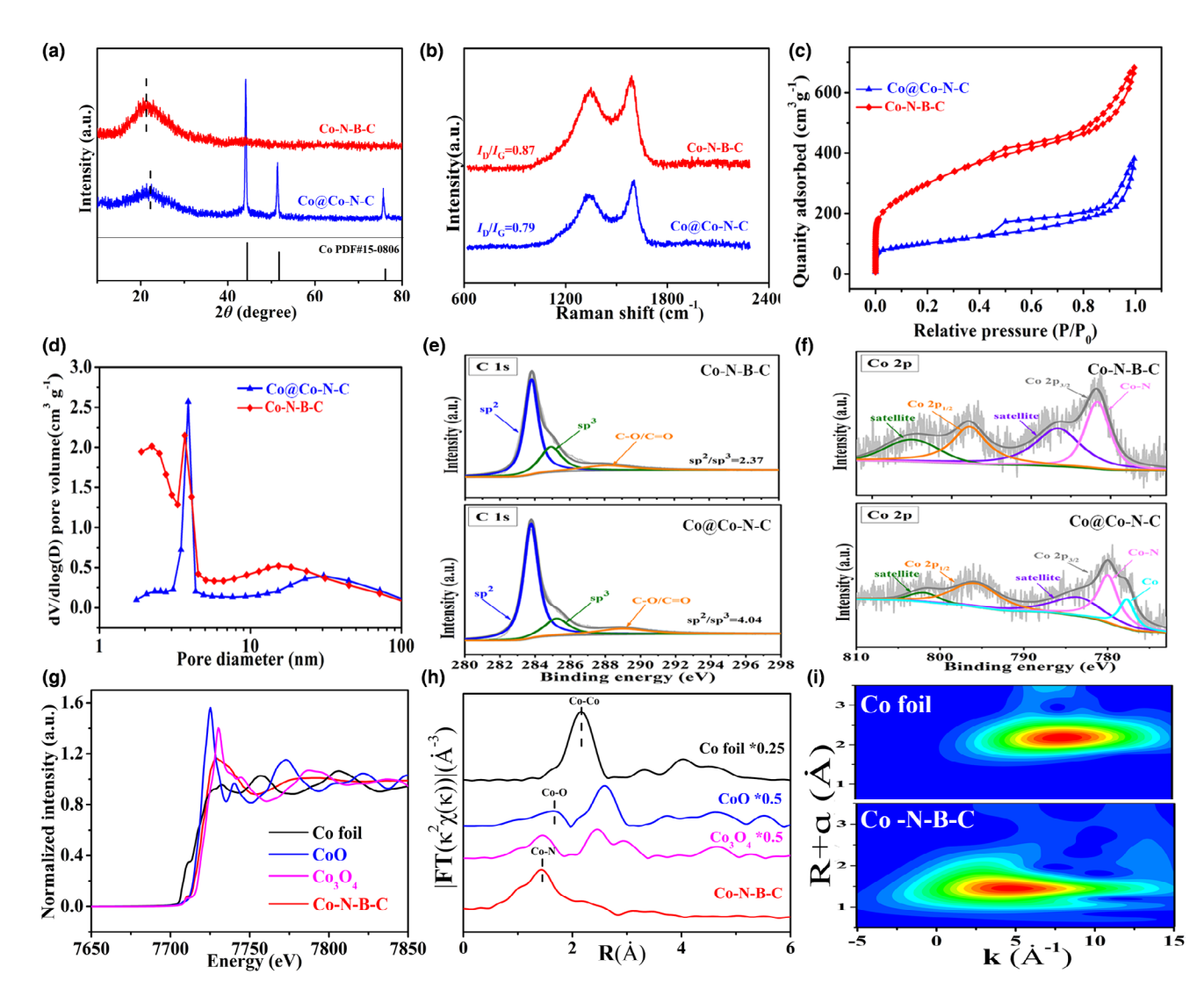


Figure 2. a) XRD patterns, b) Raman spectra and c) nitrogen adsorption/desorption isotherms and d) pore size distribution curves of Co–N–B–C and Co@Co–N–C. e) High-resolution XPS C 1s and f) Co 2p spectra of different samples. g) Co k-edge XANES spectra of Co–N–B–C and reference samples. h) Fourier transform magnitudes of k-edge EXAFS signals of Co–N–B–C and reference sample. i) Wavelet transforms for the k^2 -weighted EXAFS of Co–N–B–C and reference sample.

measurements. Co k-edge X-ray absorption near-edge structure (XANES) spectra are shown in Figure 2g. It can be seen that the adsorption edge position of Co-N-B-C is located between those of CoO and Co₃O₄, indicating single Co atom possesses positive charge and the valence of Co situates between Co²⁺ and Co³⁺. Figure 2h displays the Fourier-transformed extended X-ray absorption fine structure (EXAFS) spectra. The peak at 2.2 Å in Co foil is assigned to Co-Co coordination. [40] The Co-Co peak cannot be detected in Co-N-B-C, suggesting that Co species exist as isolated single atom. Meanwhile, the main peak of Co-N-B-C appears at 1.5 Å, corresponding to the Co-N bond. [41] The result confirms that the single Co atom is mainly stabilized by N coordination, which agrees with the aforementioned XPS analysis. As shown in Figure 2i, the wavelet transform (WT) contour plot of Co foil exhibits intensity maximum at around 6.8 Å⁻¹, corresponding to the Co-Co bond. Co-N-B-C only exhibits one intensity maximum at approximately 4.0 \mathring{A}^{-1} and the Co–Co scattering is not observed, again confirms atomic dispersion of Co atoms. [42]

2.2. Insight into the Formation Process of Co-N-B-C

All the preceding results reveal the critical role of H_3BO_3 for preparing Co–N–B–C. As is well known, H_3BO_3 as a common chemical can be dehydrated and converted to B2O3 (Figure S4a, Supporting Information). The obtained B_2O_3 can present molten fluid state during the pyrolysis process due to our set pyrolysis temperature (800 °C) is much higher than the melting point of B_2O_3 (~450 °C). First, biomass precursor can be well dispersed and then carbonized in high-temperature molten B_2O_3 media. Figure S4b, Supporting Information exhibits the SEM image of pyrolysis products without subsequent washing. It is observed that cooled B_2O_3 looks like dense cobweb, effectively enfolding and cutting carbon framework. Consequently, discontinuous carbon fragments with rich exposed edge and abundant hierarchical porous structure can be produced after removing B_2O_3 media. To better understand the effect of H_3BO_3 , the nitrogen, boron co-doped porous carbon framework (N–B–C) was prepared by identical procedure with

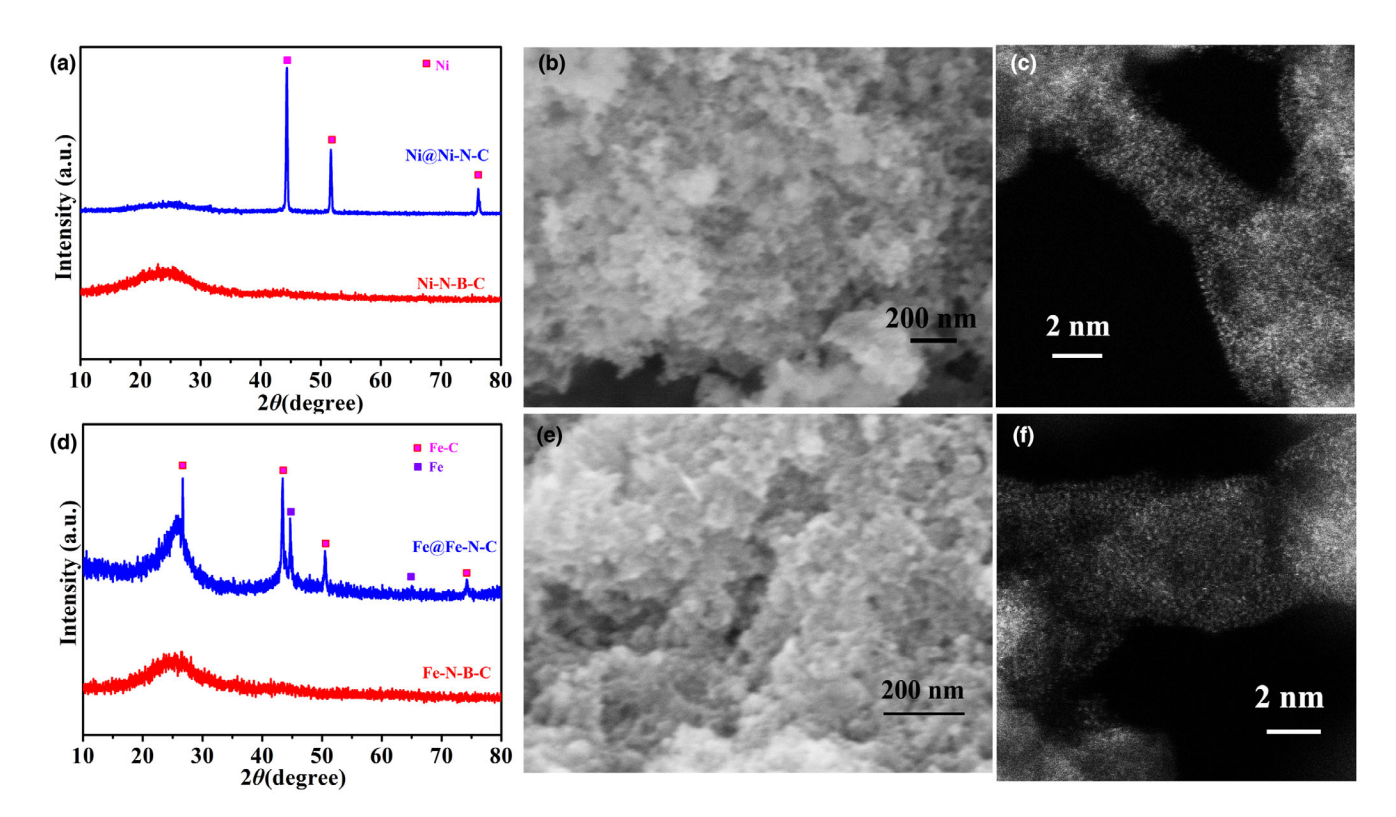


Figure 3. a, d) XRD patterns of different samples. b, c) SEM images and AC HAADF-STEM images of Ni-N-B-C and e, f) Fe-N-B-C.

only H₃BO₃ and chitosan as precursor. As shown in Figure S5a, Supporting Information, the obtained N-B-C exhibits stacked carbon nanoclusters, which is similar to that of Co-N-B-C, verifying the role of H₃BO₃ for the formation of edge-rich porous carbon matrix. The Raman spectra in Figure S5b, Supporting Information indicates relative high defect level for the N–B–C sample ($I_D/I_G = 0.84$), which is mostly related to the existence of abundant edge defects in N-B-C. The XPS survey spectrum of N-B-C in Figure S5c, Supporting Information reveals successful B doping caused by adding H₃BO₃. Clearly, the introduced H₃BO₃ plays an important role in the generation of edge-rich B-doped porous carbon matrix. Besides, the optimal concentration of H₃BO₃ was further explored. The control sample was conducted under similar conditions by altering the amount of H₃BO₃ and the corresponding products were named as Co-N-B-C-x, where x represents the mass ratio of H₃BO₃ to chitosan. As seen from the SEM images in Figure S6a, Supporting Information, it is found that the Co-N-B-C-10 sample displays lots of carbon nanoclusters along with a few carbon flakes, which is mostly due to the excessive H₃BO₃ guides the assembly of 2D carbon flakes as a hard template during the pyrolysis of chitosan. [17] In this regard, excessive H₃BO₃ is not beneficial to the formation of carbon nanoclusters, since it will further lead to the decrease in edge defects and ions transport channels. With respect to Co-N-B-C-2.5, some carbon bulks can be witnessed (see Figure S6b, Supporting Information), indicating the insufficient H₃BO₃ cannot offer enough media to disperse carbon precursor, which further results in partial aggregation of carbon matrix.

Apart from this, the blocking effect of H_3BO_3 is further explored. We only put H_3BO_3 and cobalt salt into pyrolysis treatment. It is surprised that the pyrolysis product presents light purple crystal without the formation of dark metal oxide. Furthermore, the crystal can be redissolved in the water to form clear solution (Figure S7, Supporting

Information), which illustrates molten B_2O_3 can effectively block Co species from aggregation thus facilitating the formation of single-atom Co sites. The result also verifies the recyclability of H_3BO_3 . Clearly, The formation of Co–N–B–C is mainly attributed to the special carbonization and blocking effect of molten B_2O_3 .

In order to further explore the universality of our proposed H₃BO₃assisted pyrolysis strategy, different M-N-B-C materials (M = Ni, Fe) were also fabricated by similar method using different metal precursors. It can be seen from the XRD patterns in Figure 3a,d that no metal or metal-based compound diffraction peak can be observed in Ni-N-B-C and Fe-N-B-C. The SEM images of Ni-N-B-C and Fe-N-B-C shown in Figure 3b,e confirm that their morphologies are feature with porous carbon clusters without any metal nanoparticles, which is similar to that of Co-N-B-C. As presented in Figure 3c,f, the AC HAADF-STEM images exhibit abundant high-density isolated bright dots uniformly distributing on the carbon matrix. All these results indicate that the H₃BO₃-assisted pyrolysis strategy can be also applied to successfully synthesize other atomically dispersed metal catalysts. For comparison, we also prepared the contrast samples (Ni@Ni-N-C and Fe@Fe-N-C) without adding H₃BO₃. As shown in Figure S8a,b, Supporting Information, Ni@Ni-N-C and Fe@Fe-N-C present compact carbon block. Moreover, conspicuously aggregated metal bulks can be evidenced, again suggesting the block effect of H₃BO₃. Clearly, our proposed strategy is demonstrated as a universal way to produce SACs.

2.3. ORR Performance

The ORR performance was measured by cyclic voltammogram (CV) and linear sweeping voltammetry (LSV) through three-electrode

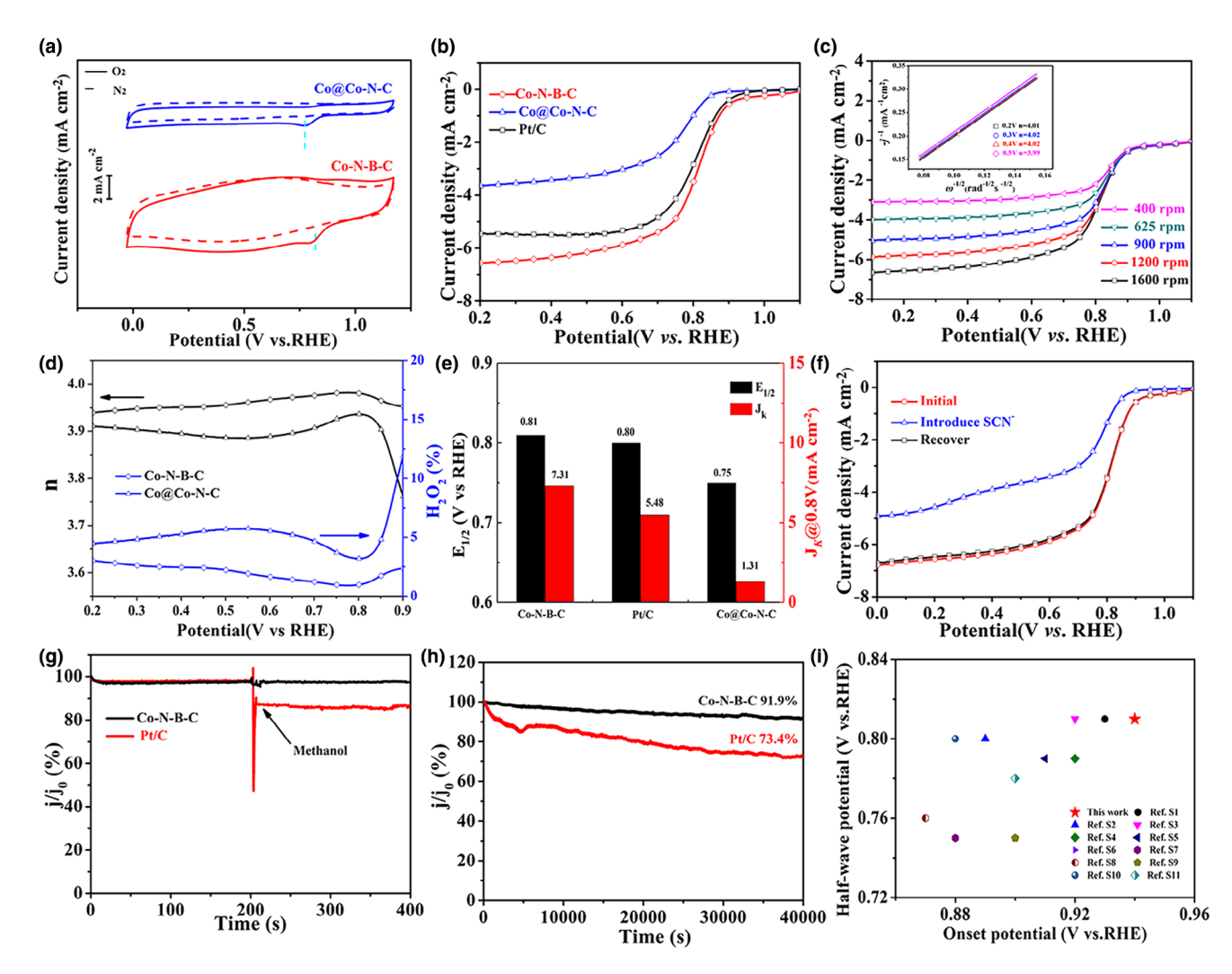


Figure 4. a) Cyclic voltammograms (CV) curves and b) linear sweep voltammograms (LSV) at 1600 rpm of Co-N-B-C, Co@Co-N-C and Pt/C. c) LSV at different rotating rate and the corresponding K-L plots (inset) of Co-N-B-C. d) Electro-transfer number and the percentage of H_2O_2 derived from the RRDE curve for Co-N-B-C and Co@Co-N-C. e) Comparison of $E_{1/2}$ and J_k for different catalyst; f) LSV curves of Co-N-B-C with and without SCN⁻ in O_2 -saturated 0.1 M KOH solution. g) Chronoamperometric response with the addition of methanol and h) regular chronoamperometric curve of Co-N-B-C and Pt/C catalyst. i) Comparison of ORR performance for the previously reported non-noble metal catalysts.

configuration in 0.1 M KOH electrolyte. As shown in Figure 4a, all the curves exhibit quasi-rectangular voltammogram. A well-designed cathodic peak could be observed after bubbling O2 until the solution is saturated. The Co-N-B-C catalyst possesses the most positive potential, which indicates its relatively better catalytic performance. To satisfy the demand for metal-air batteries, the idea cathode catalyst was required to conduct the 4e- pathway that can exhibit large current density and positive reaction potential. Figure 4b displayed the LSV curves at the rotation rate of 1600 rpm on different catalyst. The obtained Co-N-B-C catalyst exhibits the onset potential of 0.94 V and limiting current density of 6.82 mA cm⁻², outperforming the that of Pt/C catalyst $(E_{\text{onset}} = 0.91 \text{ V}, J_{\text{L}} = 6.02 \text{ mA cm}^{-2})$. It is demonstrated that Co-N-B-C catalyst with excellent ORR activity has great potential for application as cathode catalyst for metal-air batteries. In order to explore the ORR kinetics, LSV measurement with different rotation rates and the fitted K-L plots was also given in Figure 4c. The electron transfer numbers (n) of Co-N-B-C were calculated to around 4 at

different potential varying from 0.2 V to 0.5 V, suggesting its fast kinetic behavior and great selectivity in nearly four-electron transfer pathway. Meanwhile, the n can also be derivated by RRDE technique (Figure 4d). Only negligible H2O2 was yielded during the ORR on Co-N-B-C catalyst. And the calculated n for Co-N-B-C (3.98 at 0.8 V) is much larger than that for B-free Co@Co-N-C (3.91) at the same potential, again suggesting the proper electronic structure of active site in Co-N-B-C boost four-electron reduction of O2. As seen from Figure 4e, the half-potential value $(E_{1/2})$ and kinetic current density (J_k) of Co-N-B-C was 0.81 V and 7.31 mA cm⁻² respectively, much superior to other counterpart, validating the excellent ORR activity, which might be attributed to improvement in the dispersion of the Co-N_x sites and promotion of the cleaving of oxygen bond by the boron atom as suggested from the above results. [19,43] SCN poisoning experiment (Figure 4f) was tested to determine the important role of the Co atom in Co-N-B-C. When adding a content of KSCN into the electrolyte, the half potential appeared obvious negative shift and

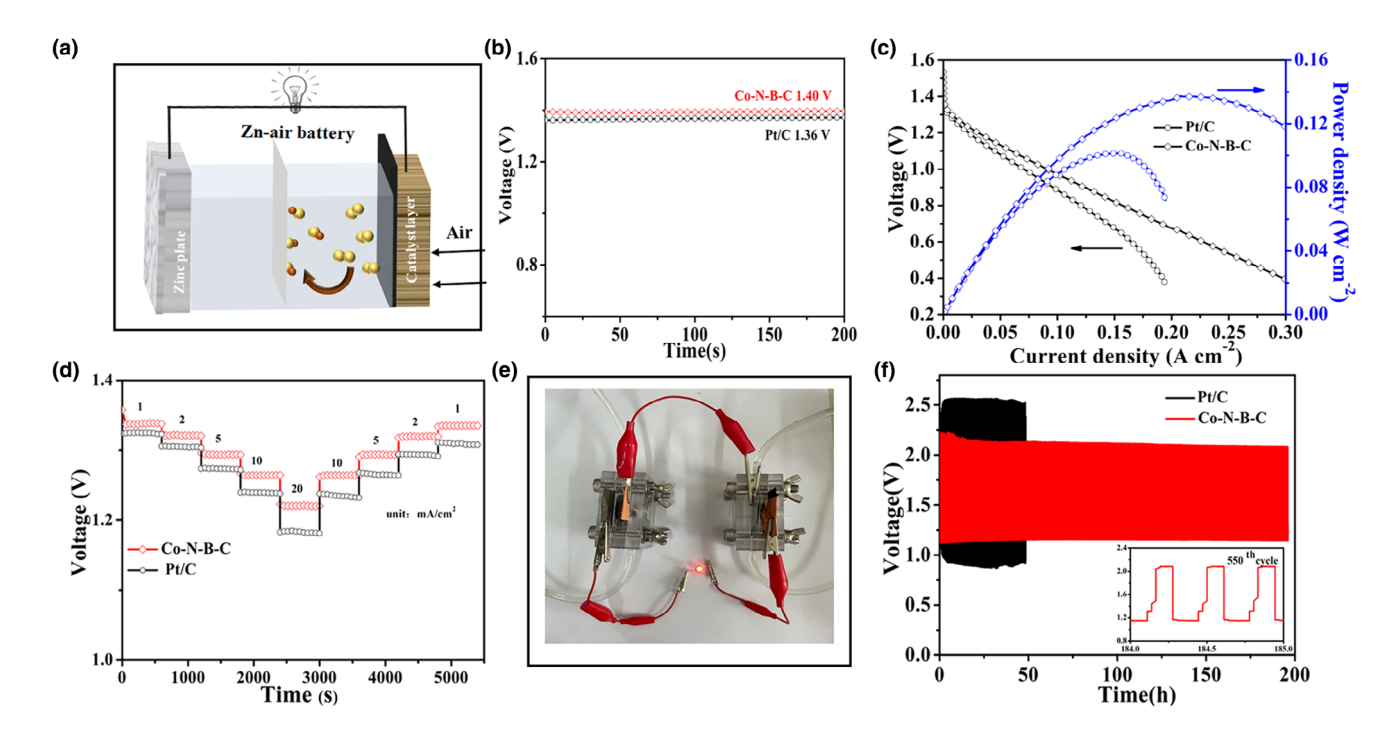


Figure 5. a) Schematic representation of the liquid Zn-air battery. b) Open-circuit voltage, c) discharge polarization and the corresponding power density curve and d) rate performance of the primary Zn-air batteries driven by Co–N–B–C and Pt/C catalyst. e) A LED bulb (>3 V) was lighted by two series-connected ZABs. f) Cycling performance and 550th galvanostatic discharge/charge curve (inset) at current density of 5 mA cm⁻² for Co–N–B–C catalyst-based ZABs.

diffusion-limiting current was significantly suppressed. After removing the SCN⁻ ion, the ORR catalytic activity was recovered, suggesting the Co atoms take great responsibility to form active sites.^[44] The durability and methanol tolerance of Co-N-B-C catalyst was conducted by chronoamperometric technique. Clearly, in contrast to the 15% current loss of Pt/C, Co-N-B-C catalysts delivered stable amperometric response (Figure 4g), thus illustrating superior tolerance towards methanol. [45] Additionally, negligible degradation can be observed after long-term cycles in Figure 4h, indicating the excellent stability of Co-N-B-C. Furthermore, the Co-N-B-C catalyst after cycling was also characterized by SEM and AC-STEM technique, as exhibited in Figure S9, Supporting Information. It can be seen that the original edge-rich porous structure and high-loading Co single atom can be well maintained even after long-term cycling test, again suggesting the favorable stability of Co-N-B-C. By comparison, the catalytic performance of Co-N-B-C still has competitive with other non-precious metal electrocatalysts reported to date (Figure 4i). More details were list in Table S1, Supporting Information.

2.4. Zn-Air Performance

To further explore the practical application of Co–N–B–C catalyst, we constructed ZABs using Co–N–B–C catalyst as air cathode on basic of the assembled configuration diagram (**Figure 5**a). It is founded that the obtained ZABs delivered high open-circuit potential of 1.40 V, even higher than that of benchmark Pt/C catalyst (Figure 5b). Figure 5c depicted that polarization and power density curves of ZABs using different catalyst. It is observed that the peak power density of Co–N–B–C

is 137.4 mW cm⁻² at 208.1 mA cm⁻², surpassing that of Pt/C (101.4 mW cm⁻² at 153.2 mA cm⁻²), which demonstrated its overwhelming electrocatalytic performance. Furthermore, the Co-N-B-C catalyst-based ZABs can output steadily potential of ~1.28 V at 5 mA cm $^{-2}$ and \sim 1.2 V at the current density of 20 mA cm $^{-2}$ respectively until the Zn plate was completely consumed (Figure S7, Supporting Information). And there is only a small voltage variation when the current density increases from 1 to 20 mA cm⁻². The voltage will recover to 1.34 V when the current density adjusts back the initial value of 1 mA cm⁻², demonstrating the excellent rate performance and stability (Figure 5d). To verify the promising practicality, ZABs driven by Co-N-B-C catalyst can be used to run a fun (Video S1, Supporting Information). Two ZABs connected in series can supply adequate power to light up Light Emitting Diodes (LED, 3 V) bulb (Figure 5e). Importantly, the Co-N-B-C catalyst-based ZABs presented excellent cyclic durability. Figure 5f showed that the discharge and charge voltage of the prepared ZABs can still keep 1.15 and 2.08 V respectively after 550 cycles, again attesting its potential to undertake a highperformance cathode catalyst in rechargeable ZABs.

In order to satisfy the demand of portable power supply device, flexible ZABs with solid-state electrolyte were also assembled. As shown in **Figure 6a**, it delivered high open circuit voltage of 1.37 V. One solid-state ZABs fabricated with Co–N–B–C catalyst can be enough to power a light board and a small working fun (Figure 6b,c), which is clearly proven the potential of practice application. Furthermore, two ZABs in series can light up an orange LED (3 V) brightly (Figure 6d). Additionally, a mobile phone can be charging by the power supply from the assembled ZABs in series (Figure 6e), further corroborating that the synthesized Co–N–B–C electrocatalysts was one of prospective cathodes for the Zn-air battery.

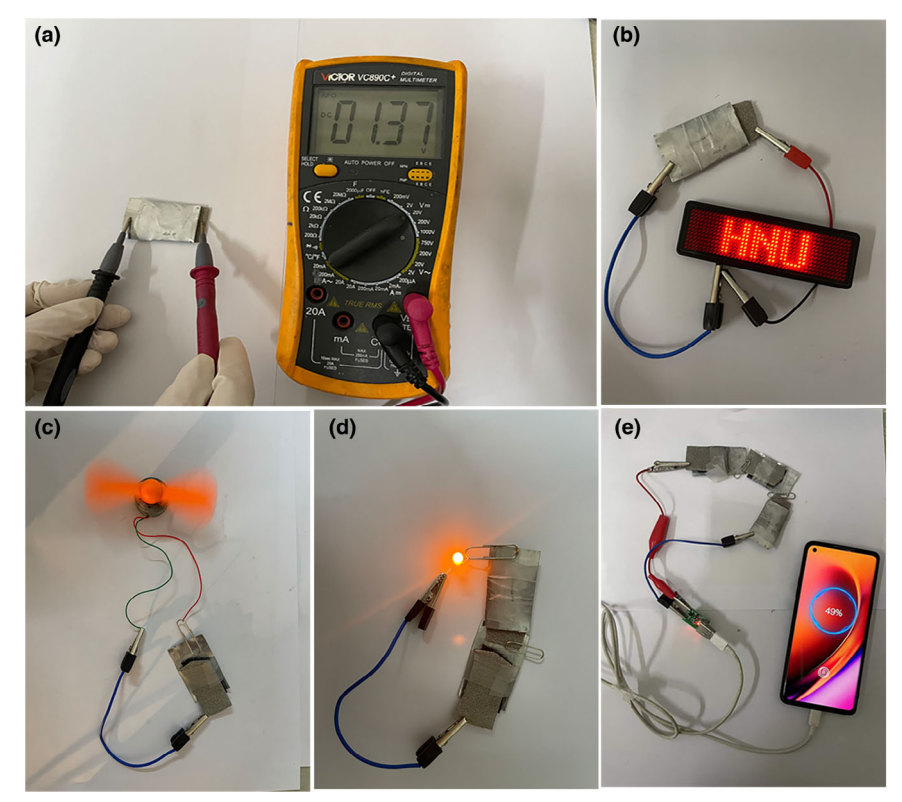


Figure 6. a) The open circuit potential of the solid-state Zn-air battery based on Co-N-B-C catalyst. b) One solid-state Zn-air battery powered a light board and c) a small working fun. d) Two solid-state Zn-air batteries in series can light up an orange LED bulb brightly. e) Three solid-state Zn-air batteries in series was charging the mobile phone.

originates from the dissolution of B_2O_3 intermediate in deionized water can be recycled and reused for the next preparation procedure.

For comparison, Co@Co–N–C and N–B–C were also synthesized by similar procedure under the condition of without adding H_3BO_3 and cobalt nitrate hexahydrate, respectively. Co–N–B–C–x were also fabricated under similar conditions except for changing the amount of H_3BO_3 . Herein, x represents the mass ratio of the H_3BO_3 to chitosan. Besides, Fe–N–B–C and Ni–N–B–C could be prepared via similar method by replacing the cobalt nitrate hexahydrate with ferric nitrate nonahydrate and nickel nitrate hexahydrate, respectively. Fe@Fe–N–C and Ni@Ni–N–C were also fabricated under the condition of no adding H_3BO_3 .

Acknowledgements

This work was supported by National Natural Science Foundation of China (Nos. 52274298, 51974114, 51672075 and 21908049), China Postdoctoral Science Foundation (2020M682560), International Postdoctoral Exchange Fellowship Program (Grant No. PC2022020), Science & Technology innovation program of Hunan province (2020RC2024 and 2022RC3037), Hunan Provincial Natural Science Foundation of China (No. 2020JJ4175), Science & Technology talents lifting project of Hunan Province (No. 2022TJ-N16), and Scientific Research Fund of Hunan Provincial Education Department (No. 21A0392).

Conflict of Interest

The authors declare no conflict of interest

3. Conclusion

In summary, a facile and green H_3BO_3 -assisted pyrolysis strategy can be employed to prepare high-loading single-atom Co–N–B–C catalyst. The results evidence the important roles of molten boron source in the preparation of Co–N–B–C. Owing to the multiple functions (special high-temperature carbonization and blocking effect), the resultant Co–N–B–C not only presents hierarchical porous structure, large SSA and abundant carbon edges but also possesses high-loading Co single atom (4.2 wt.%). Benefitting from these intriguing features, the Co–N–B–C displays outstanding performance for oxygen reduction reaction. When employed as the cathode catalyst for Zn-air batteries, it also presents remarkable electrochemical performance. Clearly, our results not only uncover the role of H_3BO_3 but also provide a promising way to massively produce high-performance SACs from low-cost biomass resources.

4. Experimental Section

Synthesis of Co–N–B–C: First, 0.5 g of chitosan and 0.1 mmol of cobalt nitrate hexahydrate were dispersed into deionized water under stirring condition. Subsequently, 2.5 g of $\rm H_3BO_3$ was slowly added. After continuous stirring for 1 h, the above solution was heated to evaporate the water, and the resultant solid powder was then pyrolyzed at 800 °C for 2 h in $\rm N_2$ atmosphere. The obtained pyrolytic product was washed by deionized water for several times to remove the residual $\rm B_2O_3$ intermediate. As a result, the final target sample, Co–N–B–C was obtained. Herein, we should point out that the remaining $\rm H_3BO_3$ aqueous solution that

Supporting Information

Supporting Information is available from the Wiley Online Library or from the author.

Keywords

boric acid, oxygen reduction reaction, single-atom catalysts, Zn-air batteries

Received: September 28, 2022 Revised: November 7, 2022 Published online: November 10, 2022

- M. Jiang, J. Yang, J. Ju, W. Zhang, L. He, J. Zhang, C. Fu, B. Sun, Energy Storage Mater. 2020, 27, 96.
- [2] M. Jiang, C. Fu, R. Cheng, W. Zhang, T. Liu, R. Wang, J. Zhang, B. Sun, Adv. Sci. 2020, 7, 2000747.
- [3] J. Hu, W. Liu, C. Xin, J. Guo, X. Cheng, J. Wei, C. Hao, G. Zhang, Y. Shi, J. Mater. Chem. A 2021, 9, 24803.
- [4] C. Zhu, Q. Shi, B. Z. Xu, S. Fu, G. Wan, C. Yang, S. Yao, J. Song, H. Zhou, D. Du, S. P. Beckman, D. Su, Y. Lin, Adv. Energy Mater. 2018, 8, 1801956.
- [5] H. Xu, D. Wang, P. Yang, A. Liu, R. Li, Y. Li, L. Xiao, X. Ren, J. Zhang, M. An, J. Mater. Chem. A 2020, 8, 23187.
- [6] A. A. Eissa, S. G. Peera, N. H. Kim, J. H. Lee, J. Mater. Chem. A 2019, 7, 16920.

- [7] H. Li, Y. Wen, M. Jiang, Y. Yao, H. Zhou, Z. Huang, J. Li, S. Jiao, Y. Kuang, S. Luo, Adv. Funct. Mater. 2021, 31, 2011289.
- [8] F. Li, G.-F. Han, H.-J. Noh, S.-J. Kim, Y. Lu, H. Y. Jeong, Z. Fu, J.-B. Baek, Energy Environ. Sci. 2018, 11, 2263.
- [9] Z. Yang, B. Chen, W. Chen, Y. Qu, F. Zhou, C. Zhao, Q. Xu, Q. Zhang, X. Duan, Y. Wu, Nat. Commun. 2019, 10, 3734.
- [10] L. Jiang, B. van Dijk, L. Wu, C. Maheu, J. P. Hofmann, V. Tudor, M. T. M. Koper, D. G. H. Hetterscheid, G. F. Schneider, ACS Catal. 2022, 12, 173.
- [11] W. Chen, X. Chen, R. Qiao, Z. Jiang, Z. Jiang, S. Papović, K. Raleva, D. Zhou, Carbon 2022, 187, 230.
- [12] S. Zhao, L. Ban, J. Zhang, W. Yi, W. Sun, Z. Zhu, Chem. Eng. J. 2021, 409, 128171.
- [13] K. Yuan, S. Sfaelou, M. Qiu, D. Lützenkirchen-Hecht, X. Zhuang, Y. Chen, C. Yuan, X. Feng, U. Scherf, ACS Energy Lett. **2018**, 3, 252.
- [14] Y. Chen, S. Ji, C. Chen, Q. Peng, D. Wang, Y. Li, Joule 2018, 2, 1242.
- [15] H. Zhou, S. Hong, H. Zhang, Y. Chen, H. Xu, X. Wang, Z. Jiang, S. Chen, Y. Liu, Appl. Catal. B Environ. 2019, 256, 117767.
- [16] Y. Zhang, L. Lu, S. Zhang, Z. Lv, D. Yang, J. Liu, Y. Chen, X. Tian, H. Jin, W. Song, J. Mater. Chem. A 2018, 6, 5740.
- [17] Z. Ling, Z. Wang, M. Zhang, C. Yu, G. Wang, Y. Dong, S. Liu, Y. Wang, J. Oiu, Adv. Funct. Mater. 2016, 26, 111.
- [18] H. Li, Y. Gong, C. Fu, H. Zhou, W. Yang, M. Guo, M. Li, Y. Kuang, J. Mater. Chem. A 2017, 5, 3875.
- [19] C. Xu, L. Chen, Y. Wen, S. Qin, H. Li, Z. Hou, Z. Huang, H. Zhou, Y. Kuang, Mater. Today Energy 2021, 21, 100721.
- [20] L. Chen, J. Feng, H. Zhou, C. Fu, G. Wang, L. Yang, C. Xu, Z. Chen, W. Yang, Y. Kuang, J. Mater. Chem. A 2017, 5, 7403.
- [21] L. Chen, Z. Chen, Y. Kuang, C. Xu, L. Yang, M. Zhou, B. He, M. Jing, Z. Li, F. Li, Z. Chen, Z. Hou, ACS Appl Mater. Interfaces 2018, 10, 27047.
- [22] P. Liu, Y. Zhao, R. Qin, S. Mo, G. Chen, L. Gu, D. M. Chevrier, P. Zhang, Q. Guo, D. Zang, B. Wu, G. Fu, N. Zheng, Science 2016, 352, 797.
- [23] Y. Wang, B. Yu, K. Liu, X. Yang, M. Liu, T.-S. Chan, X. Qiu, J. Li, W. Li, J. Mater. Chem. A 2020, 8, 2131.
- [24] L. Jiao, R. Zhang, G. Wan, W. Yang, X. Wan, W. Yang, X. Wan, H. Zhou, J. Shui, S. Yu, H. Jiang, Nat. Commun. 2020, 11, 2831.
- [25] X. Luo, M. Yang, W. Song, Q. Fang, X. Wei, L. Jiao, W. Xu, Y. Kang, H. Wang, N. Wu, W. Gu, L. Zheng, L. Hu, C. Zhu, Adv. Funct. Mater. 2021, 31, 2101193.
- [26] X. Yang, Y. Wang, G. Zhang, L. Du, L. Yang, M. Markiewicz, J. Choi, R. Chenitz, S. Sun, Appl. Catal. B Environ. 2020, 264, 118523.

- [27] F. Kong, Y. Qiao, C. Zhang, X. Fan, A. Kong, Y. Shan, Nano Res. 2020, 13, 401.
- [28] C. Li, Z. Yu, H. Liu, M. Xiong, Chem. Eng. J. 2019, 371, 433.
- [29] Z. Tan, H. Li, Q. Feng, L. Jiang, H. Pan, Z. Huang, Q. Zhou, H. Zhou, S. Ma, Y. Kuang, J. Mater. Chem. A 2019, 7, 1607.
- [30] F. Jaouen, M. Lefèvre, J. P. Dodelet, M. Cai, J. Phys. Chem. B 2006, 110, 5553.
- [31] Q. Lai, L. Zheng, Y. Liang, J. He, J. Zhao, J. Chen, ACS Catal. 2017, 7, 1655
- [32] X. Wu, L. R. Radovic, J. Phys. Chem. A 2004, 108, 9180.
- [33] D. W. Wang, D. Su, Energy Environ. Sci. 2014, 7, 576.
- [34] D. Yan, Y. Li, J. Huo, R. Chen, L. Dai, S. Wang, Adv. Mater. 2017, 29, 1606459.
- [35] L. Qie, Y. Lin, J. W. Connell, J. Xu, L. Dai, Angew. Chem. Int. Ed. 2017, 56, 6970.
- [36] C. C. Hou, L. Zou, L. Sun, K. Zhang, Z. Liu, Y. Li, C. Li, R. Zou, J. Yu, Q. Xu, Angew. Chem. Int. Ed. 2020, 59, 7384.
- [37] Y. He, S. Hwang, D. A. Cullen, M. A. Uddin, L. Langhorst, B. Li, S. Kara-kalos, A. J. Kropf, E. C. Wegener, J. Sokolowski, M. Chen, D. Myers, D. Su, K. L. More, G. Wang, S. Litster, G. Wu, Energy Environ. Sci. 2019, 12, 250.
- [38] Y. Tong, P. Chen, T. Zhou, K. Xu, W. Chu, C. Wu, Y. Xie, Angew. Chem. Int. Ed. 2017, 56, 7121.
- [39] Y. Guo, P. Yuan, J. Zhang, Y. Hu, I. S. Amiinu, X. Wang, J. Zhou, H. Xia, Z. Song, Q. Xu, S. Mu, ACS Nano 2018, 12, 1894.
- [40] R. Liu, Z. Gong, J. Liu, J. Dong, J. Liao, H. Liu, H. Huang, J. Liu, M. Yan, K. Huang, H. Gong, J. Zhu, C. Cui, G. Ye, H. Fei, Adv. Mater. 2021, 33, 2103533.
- [41] Y. Chen, R. Gao, S. Ji, H. Li, K. Tang, P. Jiang, H. Hu, Z. Zhang, H. Hao, Q. Qu, X. Liang, W. Chen, J. Dong, D. Wang, Y. Li, *Angew. Chem. Int. Ed.* 2021, 60, 3212.
- [42] H. Fei, J. Dong, C. Wan, Z. Zhao, X. Xu, Z. Lin, Y. Wang, H. Liu, K. Zang, J. Luo, S. Zhao, W. Hu, W. Yan, I. Shakir, Y. Huang, X. Duan, Adv. Mater. 2018, 30, 1802146.
- [43] J. Wu, H. Zhou, Q. Li, M. Chen, J. Wan, N. Zhang, L. Xiong, S. Li, B. Y. Xia, G. Feng, M. Liu, L. Huang, Adv. Energy Mater. 2019, 9, 1900149.
- [44] X. Yang, X. Zheng, H. Li, B. Luo, Y. He, Y. Yao, H. Zhou, Z. Yan, Y. Kuang, Z. Huang, Adv. Funct. Mater. 2022, 32, 2200397.
- [45] K. Li, C. Wang, H. Li, Y. Wen, F. Wang, Q. Xue, Z. Huang, C. Fu, ACS Appl Mater. Interfaces 2021, 13, 47440.